A probabilistic bulk model of coupled mixed layer and convection. Part II: Shallow convection case

P. Gentine, A.K. Betts, B.R. Lintner, K.L. Findell, C.C. van Heerwaarden, Fabio d'Andrea

A Probabilistic Bulk Model of Coupled Mixed Layer and Convection. Part II: Shallow Convection Case

PIERRE GENTINE,* ALAN K. BETTS,[+] BENJAMIN R. LINTNER,[#] KIRSTEN L. FINDELL,[@]
CHIEL C. VAN HEERWAARDEN,[&] AND FABIO D'ANDREA**

* Columbia University, New York, New York
[+] Atmospheric Research, Pittsford, Vermont
[#] Rutgers, The State University of New Jersey, New Brunswick, New Jersey
[@] Geophysical Fluid Dynamics Laboratory, Princeton, New Jersey
[&] Max Planck Institute for Meteorology, Hamburg, Germany
** Laboratoire de Meteorologie Dynamique, Paris, France

ABSTRACT

The probabilistic bulk convection model (PBCM) developed in a companion paper is here extended to shallow nonprecipitating convection. The PBCM unifies the clear-sky and shallow convection boundary layer regimes by obtaining mixed-layer growth, cloud fraction, and convective inhibition from a single parameterization based on physical principles. The evolution of the shallow convection PBCM is based on the statistical distribution of the surface thermodynamic state of convective plumes.

The entrainment velocity of the mixed layer is related to the mass flux of the updrafts overshooting the dry inversion capping the mixed layer. The updrafts overcoming the convective inhibition generate active cloud-base mass flux, which is the boundary condition for the shallow cumulus scheme. The subcloud-layer entrainment velocity is directly coupled to the cloud-base mass flux through the distribution of vertical velocity and fractional cover of the updrafts.

Comparisons of the PBCM against large-eddy simulations from the Barbados Oceanographic and Meteorological Experiment (BOMEX) and from the Southern Great Plains Atmospheric Radiation Measurement Program (ARM) facility demonstrate good agreement in terms of thermodynamic structure, cloud-base mass flux, and cloud top.

The equilibrium between the cloud-base mass flux and rate of growth of the mixed layer determines the equilibrium convective inhibition and cloud cover. This process is an important new insight on the coupling between the mixed-layer and cumulus dynamics. Given its relative simplicity and transparency, the PBCM represents a powerful tool for developing process-based understanding and intuition about the physical processes involved in boundary layer–convection interactions, as well as a test bed for diagnosing and validating shallow convection parameterizations.

1. Introduction

Boundary layer clouds play a major role in the climate system through modification of the radiative budget and hydrologic cycle (Klein and Hartmann 1993; Bechtold and Siebesma 1998; Bretherton et al. 2004). Low-level clouds remain the largest source of uncertainty in climate models and have a significant impact on both Earth's radiative budget and the associated heat transport (Bony et al. 2006; Donohoe and Battisti 2012). This large uncertainty is due to the representation of low clouds, which are inherently small-scale features (100 m to a few kilometers), on the coarser-resolved scales of climate models (100 km). Consequently, the cloud cover and the processes associated with cloud formation have to be parameterized as a function of the larger-scale variables (e.g., Bony and Emanuel 2001).

In recent decades, fundamental advances have been made in our physical understanding and representation of moist convection through: intensive observational campaigns, such as the Global Atmospheric Research Program (GARP) Atlantic Tropical Experiment (GATE) (Betts 1974), the Barbados Oceanographic and

Meteorological Experiment (BOMEX) (Holland 1971), the Atlantic Trade Wind Experiment 1969 (ATEX) (Brocks et al. 1970), and the Atmospheric Radiation Measurement Program (ARM) (Revercomb et al. 2003); high-resolution modeling with large-eddy simulations (Brown et al. 2002; Siebesma et al. 2003); improvements in the parameterizations used in single-column and global climate models (Betts 1986; Betts and Miller 1986; Tiedtke 1989; Emanuel 1991; von Salzen and McFarlane 2002; Golaz et al. 2002a,b; Brown et al. 2002; Siebesma et al. 2003; Bretherton et al. 2004; McCaa and Bretherton 2004; Neggers 2009; Neggers et al. 2009); as well as idealized, bulk representations of moist convection (Betts 1973, 1975; Albrecht et al. 1979; Albrecht 1984; Betts 1985; Zhu and Albrecht 2002; Bellon and Stevens 2005; Stevens 2006; Khouider and Majda 2006; Bretherton and Park 2008; Majda and Stechmann 2008; Khouider et al. 2010; Lintner et al. 2013). The latter approaches have been important steps toward the development of our understanding of the physical processes associated with moist convection and toward the improvements of climate model parameterizations. By including a minimum yet sufficient number of processes to represent moist convective physics, such bulk formulations are computationally inexpensive and flexible, easily tuned and validated over different areas and climates, and ideally suited to test hypotheses. In fact, by limiting the processes involved, such idealized models can often cut through complicating factors (e.g., feedbacks) that obscure the interpretation of more complex models.

The representation of shallow convection dynamics remains a challenge, especially over land where rapid variations are induced by the large-amplitude diurnal radiation. Boundary layer cloud cover is linked to surface forcing (sea surface temperature over the ocean and surface heat fluxes over land), lower-tropospheric stability, surface pressure, and subsidence but the interplay among these mechanisms is still a challenging issue (Klein and Hartmann 1993; Bechtold and Siebesma 1998). As an example, a critical deficiency of current-generation climate models is the incorrect phasing of diurnal precipitation occurrence over land, with many models triggering deep convection too early in the day. The temporal coevolution of shallow convection and surface and large-scale forcing is likely to be important for preconditioning the atmosphere and initiating deep convection (Guichard et al. 2004, 2009). Specific issues that have to be addressed are related to the formulation of the mass flux, cloud fraction, radiative feedback, entrainment parameterization of both the mixed layer and cloud layer, and the coupling between the mixed layer and cloud layer above it.

To address the interplay of shallow convection and the boundary layer, we extend a novel bulk formulation

developed in a companion paper (Gentine et al. 2013): the probabilistic-bulk convection model (PBCM). The principal advance in PBCM is that the active convection (defined as the buoyant part of moist convection) and the entrainment velocity of the dry mixed layer are related to the mass flux of updrafts in the inversion capping the mixed layer. Indeed, the clear-sky entrainment velocity introduced in Gentine et al. (2013) is naturally extended to the top of the subcloud layer in the presence of active moist convection. In our formulation of PBCM, the updraft mass flux, convective inhibition (CIN), rate of growth of the subcloud layer, and cloud fraction are intimately linked to the surface state distribution of conserved variables, liquid potential temperature θ_l, and total specific humidity q_{tot}. In this regard, our work extends the recent developments toward a unified convective scheme (e.g., Bretherton et al. 2004; McCaa and Bretherton 2004; Bretherton and Park 2009).

In what follows, we construct a unified formulation of the entrainment velocity of the subcloud layer and cloud-base active mass flux. This formulation is then tested against large-eddy simulation (LES) results for steady-state trade wind cumulus conditions from BOMEX (Siebesma et al. 2003) and for the dry-to-shallow-convection transition over land, which is based on an idealization of observations made at the Southern Great Plains (SGP) site of ARM on 21 June 1997 (Brown et al. 2002).

2. Model assumptions and structure

a. Boundary layer profile

In what follows, all updrafts are assumed to originate from the surface. We distinguish two types of shallow convection: forced and active. "Forced shallow convection" refers to moist convection generated by thermals that overshoot the dry inversion layer but which, because of their negative buoyancy above the lifting condensation level (LCL), ultimately sink back into the mixed layer. These thermals reach their LCL but not their level of free convection (LFC). "Active shallow convection" refers to moist convection generated by thermals that are positively buoyant (conditionally unstable) above the LCL (Stull 1988); having overcome their CIN, active convection thermals reach their LFC and ultimately leave the subcloud system.

In the presence of active convection, the moist boundary layer has a structure described in Fig. 1. The model profile is presented for virtual potential temperature θ_v. The subcloud layer is approximated with a first-order model. The bulk model is divided into six continuous regions:
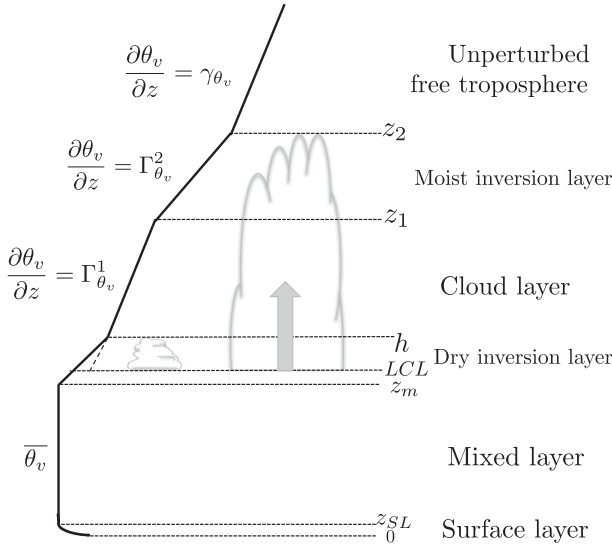
FIG. 1. Moist boundary layer structure in virtual potential temperature.

1) The surface layer extending from the surface to height $z_{SL} = 0.1z_m$. In this region the temperature and humidity profiles are logarithmic, with a stability correction following Beljaars and Holtslag (1991).

2) The mixed layer extending from z_{SL} to z_m in which θ and q are assumed to be uniform in z, equal to $\overline{\theta}$ and $\overline{q}$.

3) A so-called "dry" inversion layer between z_m and h caps the dry mixed layer. In the presence of shallow convection, the LCL is located within this dry inversion layer and forced clouds are present.

4) The ensemble of active clouds creates a cloud layer extending from the LCL to z_1. The dry inversion top lies above the LCL, pointing to the presence of forced clouds. The cloud layer has constant lapse rates Γ_θ^1 for potential temperature and Γ_q^1 for specific humidity between h and z_1. The layer is conditionally unstable.

5) Above the cloud layer lies the moist inversion layer, extending between z_1 and z_2, with a stable profile. This layer is characterized by constant lapse rates Γ_θ^2 for potential temperature and Γ_q^2 for specific humidity.

6) The region above z_2 corresponds to the unperturbed region of the free-tropospheric profile, where the lapse rates γ_θ and γ_q of potential temperature and specific humidity, respectively, are specified. These lapse rates vary according to prescribed large-scale tendencies.

"Cumulus layer" refers to the sum of the cloud and moist inversion layers extending from LCL to z_2.

All bulk variables are assumed to represent mean-areal values, averaged across both cloudy and noncloudy regions. Since the fractional cover of active convection is small ($\leq 10\%$), the effect of liquid water is neglected in the area-averaged value of Γ_θ^1, Γ_q^1, Γ_θ^2, and Γ_q^2. This assumption is similar to most models of moist convection (e.g., Betts 1973; Arakawa and Schubert 1974; Bretherton and Park 2008).

Prognostic equations for the bulk model state variables are derived in response to surface (turbulent heat fluxes) and large-scale forcing (low-level convergence, radiation, advection, and initial free-tropospheric profiles). The evolution of the state variables (liquid potential temperature and total specific humidity) is related to the statistical moments of these variables near the surface.

The bulk model is composed of 10 variables requiring prognostic equations:

1) $\overline{\theta}$, $\overline{q}$, and z_m in the dry region of the boundary layer.
2) h, the top of the dry inversion layer. In this layer, the temperature and humidity lapse rates are obtained by continuity of the profiles. In the case of shallow convection, the LCL is located in this layer and is diagnosed from $\overline{\theta}$ and $\overline{q}$.
3) Γ_θ^1, Γ_q^1, and z_1 in the cloud layer.
4) Γ_θ^2, Γ_q^2, and z_2 in the moist inversion layer.

The objective of our formulation is to relate the subcloud-layer entrainment velocity and active cloud-base mass flux to the updraft mass flux within the dry inversion by decomposing the mass flux into active and nonactive parts. To this end, we relate the updraft mass flux to the distribution of the conserved variables of plumes originating from the surface.

b. Conserved variables

The shallow clouds are assumed to be nonprecipitating. We consider θ_l and q_{tot} as the conserved variables of the parcels. We define θ_l as $\theta \exp(-Lq_l/C_pT)$, with L latent heat of vaporization, C_p the specific heat of air at constant pressure, but is here approximated linearly: $\theta_l \approx \theta - (L/C_p)q_l$. The total specific humidity is the sum of the water vapor and liquid specific humidity, $q_{tot} = q + q_l$. Table 1 summarizes all variables and their definitions.

c. Variability at the surface

Gentine et al. (2013) fully describes the representation of surface variability in the model. Here, only a brief summary is given for completeness. The turbulence at the bottom of the mixed layer (level z_{SL}) is represented as a joint probability distribution function (pdf) of the conserved variables (θ, q) and of the vertical turbulent velocity w. The pdf is assumed to be Gaussian (Golaz et al. 2002a; Cheinet 2003, 2004; Berg and Stull 2004; Neggers et al. 2009) and centered around the mean values of $\overline{\theta}$ and $\overline{q}$. The limitations behind this hypothesis

TABLE 1. List of variables and description.

Variable	Description	Units
B	Buoyancy of the updraft	m s^{-2}
C_p	Specific heat of dry air	J K^{-1}
f_u	Fraction cover of updrafts	—
f_a	Fraction cover of active updrafts with $\theta'_v > \theta'_{v,\text{LFC}}$	—
h	Top of dry inversion layer	m
L	Latent heat of vaporization	J kg^{-1}
LCL	Lifting condensation level	m
LFC	Level of free convection	m
M_c	Total mass flux in the cloudy region	kg m s^{-1}
M_u	Updraft mass flux	kg m s^{-1}
M_u^{active}	Active updraft mass flux	kg m s^{-1}
$M_u^{\text{nonactive}}$	Nonactive updraft mass flux	kg m s^{-1}
q	Water vapor specific humidity	kg kg^{-1}
q_l	Liquid specific humidity	kg kg^{-1}
q_{sat}	Saturation water vapor	kg kg^{-1}
q_{tot}	Total specific humidity	kg kg^{-1}
$\overline{q}$	Areal-mean value of q in the dry mixed layer	kg kg^{-1}
$\overline{q}(z)$	Areal-mean value of q at level z	kg kg^{-1}
T	Absolute temperature	K
w	Upward turbulent velocity	m s^{-1}
$\overline{w'\phi'}$	Vertical transport of conserved variable ϕ	m s$^{-1}\phi$
$\overline{X}^u$	Ensemble-mean value of variable X over the updraft ensemble	—
$\overline{X}^a$	Ensemble-mean value of variable X over the active updraft ensemble with $\theta'_v > \theta'_{v,\text{LFC}}$	—
$\overline{X}^{\text{env}}$	Ensemble-mean value of variable X over the environment	—
X'	Turbulent deviation of X around it mean statistical value $\overline{X}$	—
z_m	Mixed-layer depth	m
z_1	Cloud-layer depth	m
z_2	Moist-inversion-layer depth	m
δ	Detrainment rate of the cloud updrafts	m^{-1}
ϵ	Entrainment rate of the cloud updrafts	m^{-1}
Γ_θ^1	Potential temperature lapse rate in the cloud layer	K m^{-1}
Γ_q^1	Specific humidity lapse rate in the cloud layer	kg kg^{-1} m^{-1}
Γ_θ^2	Potential temperature lapse rate in the inversion layer	K m^{-1}
Γ_q^2	Specific humidity lapse rate in the inversion layer	kg kg^{-1} m^{-1}
ϕ	Conserved variable $\phi = \{\theta_l, q_{\text{tot}}\}$	—
ρ	Air density	kg m^{-3}
θ	Potential temperature	K
θ_l	Liquid potential temperature	K
$\theta'_{v,h}$	Minimum virtual potential temperature anomaly required to reach the top of the dry inversion h	K
$\theta'_{v,\text{LCL}}$	Minimum virtual potential temperature anomaly required to reach the LCL	K
$\theta'_{v,\text{LFC}}$	Minimum virtual potential temperature anomaly required to reach the LFC	K
$\overline{\theta}$	Areal-mean value of θ in the dry mixed layer	K
$\overline{\theta}(z)$	Areal-mean value of θ at level z	K

are discussed in detail in Gentine et al. (2013). The variances of θ, q, and w are given by similarity relationships in the surface layer and are directly related to the surface sensible and latent heat fluxes. The covariances $\overline{w\theta}$ and $\overline{wq}$ are directly related to the sensible and latent heat fluxes. The correlation between θ and q is assumed to be one for the updrafts [as in De Bruin et al. (1999)].

d. Fate of the updrafts

The updrafts, characterized by an initial virtual potential temperature anomaly $\theta'_v = \theta_v - \overline{\theta_v} > 0$, are buoyant and rise from the lowest level of the mixed layer z_{SL}.

Their dynamics is described by a plume model, which laterally entrains environmental air at rate ϵ (Betts 1973; Jakob and Siebesma 2003; de Rooy and Siebesma 2008). The fractional cover of each updraft is assumed unchanged below the LCL. In the subcloud layer, the total updraft fractional cover can nonetheless change since some parcels fall back into the mixed layer under the effect of negative buoyancy. In the cumulus layer, the fractional cover of the updrafts is modified by lateral entrainment.

If the updraft reaches its LCL, cloud cover is generated. To reach the LCL, θ'_v has to be larger than a threshold
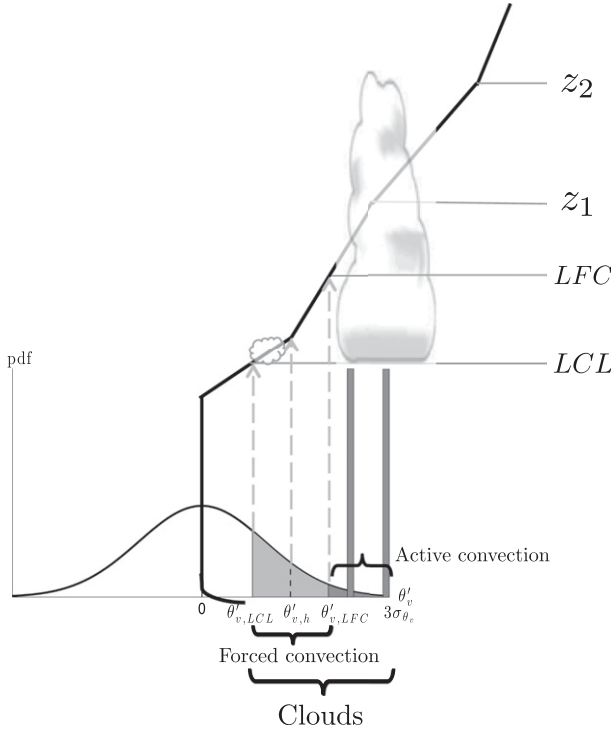
FIG. 2. Schematic representation of the lower-mixed-layer pdf and its effect on forced and active moist convection generation. Gray areas represent cloud cover (forced and active); dark gray represents active convection. The dashed arrows represent the height reached by updrafts with threshold virtual potential temperature values at the surface. A continuous pdf is used below $\theta'_{v,\text{LCL}}$. Above $\theta'_{v,\text{LCL}}$, two single plumes (dark gray bars) are used instead of the pdf tail (dark gray). A first representative plume has properties θ_l^u and q_{tot}^u averaged over the tail of the pdf for $\theta'_v > \theta'_{v,\text{LCL}}$. A second plume characterized by $3\sigma_\theta$ temperature and $3\sigma_q$ humidity is used to find the cloud top and the level of neutral buoyancy (thus defining the evolution of level z_1).

value $\theta'_{v,\text{LCL}}$. The partitioning of the updrafts based on their initial buoyancy is depicted in Fig. 2. In principle, the LCL has different values across the updraft spectrum because of varying humidity content in the updrafts. However, using a Monte Carlo technique to investigate the LCL variations across updraft parcels, we note variations less than 1%, so we neglect LCL variations here. Among the subset of updrafts reaching the LCL only a small fraction is able to reach the LFC and therefore to overcome the CIN. A CIN threshold $\theta'_{v,\text{LFC}}$ can thus be defined for the surface pdf. Above this threshold, the updrafts reach the LFC and ultimately leave the subcloud layer, generating active shallow convection. As in the dry case in Gentine et al. (2013), only the parcels with initial buoyancy anomaly larger than $\theta'_{v,h}$, the dry CIN, generate subcloud-layer entrainment velocity. Since the updrafts overcoming the CIN, characterized by $\theta'_v > \theta'_{v,\text{LFC}}$, leave the subcloud layer, only the parcels with $\theta'_{v,h} < \theta'_v < \theta'_{v,\text{LFC}}$ induce mixed-layer growth.

In summary, the updrafts can be divided into four categories, as depicted in Fig. 2:

1) If $0 < \theta'_v \leq \theta'_{v,\text{LCL}}$, the updrafts are dry and do not induce subcloud layer growth since they cannot reach h.
2) If $\theta'_{v,\text{LCL}} < \theta'_v \leq \theta'_{v,h}$, the updrafts produce condensate but do not induce subcloud layer growth since they cannot reach h. These updrafts generate forced clouds.
3) If $\theta'_{v,h} < \theta'_v \leq \theta'_{v,\text{LFC}}$, the updrafts reach both their LCL and h, and they thus produce condensate, generating forced cloud cover, and induce subcloud-layer growth. These updrafts ultimately sink back into the mixed layer.
4) If $\theta'_v > \theta'_{v,\text{LFC}}$, the updrafts become cloudy above the LCL and then reach their LFC, creating active shallow cumuli. These active updrafts leave the subcloud layer thanks to the buoyancy acquired by condensation. The leaving mass flux reduces the growth of the mixed layer compared to the dry case.

3. Method of solution

a. Overview

Figure 3 summarizes the method of solution. In both the subcloud and cumulus layers, the vertical profiles of the updraft state variables (θ_l^u, q_{tot}^u, w_u^2) are determined by an entraining plume model (see next subsection). In the subcloud layer, $z \leq \text{LCL}$, the mass flux is obtained by integration of the initial buoyancy anomaly over the updrafts reaching level z:

$$M_u(z) = \rho \int_0^\infty \max(w_u, 0) N(\theta'_v)\, d\theta'_v, \qquad (1)$$

where w_u is given by integration of the plume model and $N(\theta'_v)$ is the Gaussian distribution in virtual potential temperature anomaly at the surface. This expression has a similar flavor to the cloud-base mass-flux derivation of Bretherton et al. (2004). The semianalytical solution of Eq. (1) is relatively easy since all processes are a linear transformation of the surface Gaussian distribution in θ'_v and are therefore Gaussian.

The mass flux at $z = h$ is used to compute the entrainment velocity [see section 4d(1)]. The mass flux at cloud base (LCL) is used as the boundary condition for the cumulus scheme.

In the cumulus layer, $z \geq \text{LCL}$, the computation of the updraft characteristics is complicated by the nonlinear condensation process. Consequently, instead of considering the whole pdf, we only use two diagnostic "Dirac" plumes [as in Neggers (2009) and Neggers et al. (2009)], which sample the tail ($\theta'_v > \theta'_{v,h}$) of the surface pdf. These two plumes, represented by two bars in Fig. 2, are
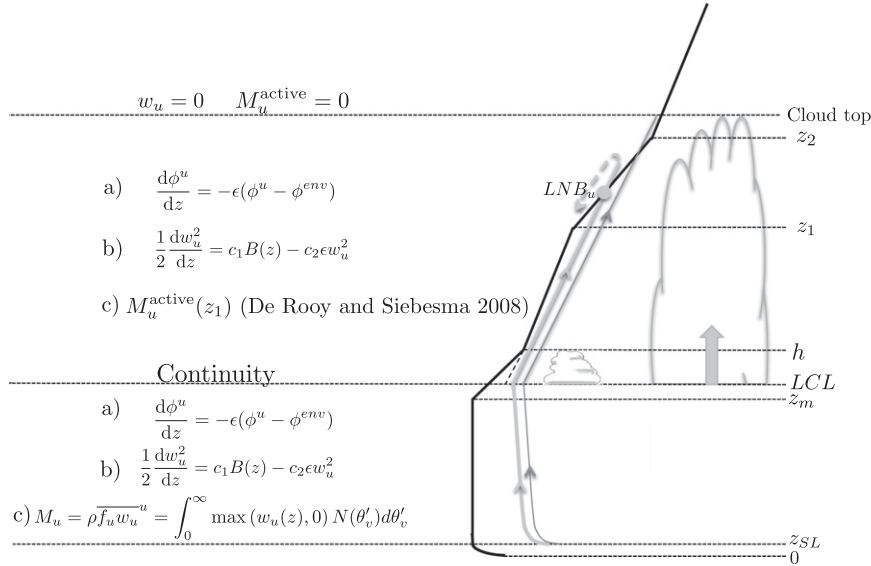
FIG. 3. Schematic describing how the model resolves the updrafts in the subcloud layer below the LCL and in the cloud layer. In the subcloud layer, the entire pdf is used to find the conserved variables (step a), vertical velocity (step b), and then the mass flux (step c) by integration over the pdf over only the positive vertical velocity values. In the cloud layer, only two plumes are used: a diagnostic-mean plume (light thick gray arrow) and the most energetic $3\sigma_{\theta_v}$ updraft (thin dark gray arrow). This latter energetic updraft is used to define the cloud top and level z_1.

1) a "bulk diagnostic" updraft representative of the conditions averaged over the tail of the distribution, used to define the convective transport. This updraft defines the cloud-layer top z_1 at its level of neutral buoyancy (LNB).

2) A dominant-mode entraining plume, with $3\sigma_{\theta_v}$ initial anomaly, in which the overshoot determines the top of the moist inversion, as the cloud top.

b. Turbulent transport in the subcloud and cumulus layers

1) PLUME MODEL

The moist-conserved variables of the updrafts are computed using a single entraining plume model (Simpson et al. 1965; Simpson and Wiggert 1969; Betts 1975; Siebesma et al. 2003; Bretherton and Park 2008):

$$\frac{d\phi^u}{dz} = -\epsilon(\phi^u - \phi^{\text{env}}), \qquad (2)$$

$$\frac{1}{2}\frac{dw_u^2}{dz} = c_1 B(z) - c_2 \epsilon w_u^2, \qquad (3)$$

where ϕ^u refers to the moist-conserved variables of the updraft (i.e., $\{\theta_l, q_{\text{tot}}\}$) and ϕ^{env} refers to the conserved variables of the environment, $c_1 = 1/3$ and $c_2 = 2$ as in

Jakob and Siebesma (2003) and $B(z) = (g/\theta_v^{\text{env}})(\theta_v^u - \theta_v^{\text{env}})$ is the updraft buoyancy. Since the fractional cover of moist convection is small, the liquid water content effect on the environmental value is neglected so that $\phi^{\text{env}} = \{\theta^{\text{env}}, q^{\text{env}}\}$. In addition, the environmental values can be approximated by the areal-mean value $\overline{\phi}(z) = \{\overline{\theta}(z), \overline{q}(z)\}$, the averaged value at level z.

Once the conserved variables of the updrafts θ_l^u and q_{tot}^u are determined, the potential temperature θ^u, water vapor specific humidity q^u, and virtual potential temperature θ_v^u are found after calculation of the moist adiabatic and the saturation specific humidity $q^*(T, P)$ (see appendix A), assuming that the water vapor specific humidity q^u is equal to its saturation value (i.e., no supersaturation).

In the cumulus layer, the entrainment rate formulation of de Rooy and Siebesma (2008), $\epsilon = c_\epsilon/z$ with $c_\epsilon = 1$. In the subcloud layer, the lateral entrainment is assumed to scale with the height of the mixed layer with a similar equation $\epsilon = c_\epsilon/z_m$. In the subcloud layer, the vertical velocity $w_u(z)$ is solved analytically [as in Gentine et al. (2013)] by first solving the conserved variables $\phi^u(z)$ and buoyancy anomaly. The fraction of updrafts at level z, $f_u(z)$ is then given as the probability of updrafts reaching level z. The corresponding mass flux is thus known analytically at all levels until cloud base.

2) TRANSPORT IN THE CUMULUS LAYER: MASS FLUX

The turbulent transport in the cumulus layer is assumed to be dominated by the updraft transport (Soares et al. 2004; Bretherton et al. 2004). The downdraft mass flux is negligible at LCL for nonprecipitating shallow convection. The turbulent transport is described by a mass-flux approximation (Betts 1975; Siebesma et al. 2003; Bretherton and Park 2008), in which a single diagnostic plume (Fig. 2) is used:

$$\rho \overline{w'\phi'} = M_u^{\text{active}}(\phi^u - \phi^{\text{env}}). \tag{4}$$

In our bulk model we only need to find the turbulent transport at levels LCL, z_1, and z_2. The turbulent transport at the LCL is obtained by continuity of the clear boundary layer transport. At the cumulus top z_2, the updraft transport vanishes since the velocity vanishes. Therefore the transport only needs to be specified at the bottom of the moist inversion z_1. This allows some simple and robust sensitivity test on the effect of the transport partitioning between the cloud and moist inversion layers (e.g., owing to different detrainment parameterizations).

Our estimate of the detrainment is based on the scheme of de Rooy and Siebesma (2008). In this formulation the detrainment rate is time varying and depends on the cloud height. This parameterization is attractive since it is both analytical and capable of realistically representing a wide range of observed mass-flux profiles from the shallowest to the tallest clouds. In this formulation the updraft mass-flux profile is exponentially decreasing until a reference level z^* and then decreases linearly to vanish at cloud top. Between LCL and z^* (de Rooy and Siebesma 2008), the updraft mass-flux profile is

$$M_u^{\text{active}}(z) = M_u^{\text{active}}(\text{LCL})\left(\frac{z}{\text{LCL}}\right)^{c_\epsilon} e^{-\delta(z-\text{LCL})}, \tag{5}$$

where the boundary condition $M_u^{\text{active}}(\text{LCL})$ will be computed in the next section. The detrainment δ depends on the critical mixture χ_s of environmental air required to obtain neutral buoyancy of the updraft, at level z^*. Detrainment is uniform below z^* and z dependent above it to satisfy the linear decay of the mass flux.

In their original derivation, de Rooy and Siebesma (2008) used the middle of the cloud (LCL + cloud top)/2 as z^*. In the early stage of shallow convection, the updraft buoyancy is negative at midcloud level. The level

of neutral buoyancy of the updraft is located below midcloud. Consequently, χ_s is undefined. To correct this undesirable effect we define χ_s at a new $z^* = (\text{LNB} + \text{LCL})/2$—that is, at midpoint within the cloud layer where the updraft is always positively buoyant by construction. This modified formulation better describes the cloud dynamics in the early stage of shallow convection development. The mass-flux profile is only evaluated at z_1 (i.e., within the linearly decaying part of the profile).

3) BOUNDARY CONDITION AT LCL: CONNECTION BETWEEN SUBCLOUD AND CUMULUS LAYERS

The bulk-diagnostic updraft is by definition the mean of all active updrafts (i.e., those overcoming the CIN). Its conserved variables $\overline{\phi^u}^a$ are obtained by integration of the surface pdf over the active part, $\theta'_v > \theta'_{v,\text{LFC}}$—that is, the dark gray area in Fig. 2. The term $\overline{X}^a$ represents the conditional average of X over the active updrafts with initial $\theta'_v > \theta'_{v,\text{LFC}}$. This conditional average can be solved analytically and gives

$$\overline{\phi^u}^a = \overline{\phi} + \Gamma_{z_m}^{\phi}\left(z - z_m - \frac{1}{\epsilon}\right)$$
$$+ \exp[-\epsilon(z - z_m)]\frac{\Gamma_{z_m}^{\phi} + \epsilon \exp(-\epsilon z_m)\overline{\phi_0^u}^a}{\epsilon}, \tag{6}$$

with

$$\overline{\phi_0^u}^a = \frac{\sigma_\phi}{\sqrt{2\pi}}\exp\left(-\frac{1}{2}\phi_{\text{LFC}}'^2\sigma_\phi^2\right), \tag{7}$$

and $\phi'_{\text{LFC}} = \sigma_\phi/\sigma_{\theta_v}\theta'_{v,\text{LFC}}$ by linearity of the Gaussians and unit surface correlation between q and θ.

The updraft mass flux is found by continuity at LCL and is calculated by averaging the vertical velocity w_u of the active updrafts emerging from the mixed layer:

$$M_u^{\text{active}}(\text{LCL}) = \rho f_a \overline{w_u(\text{LCL})}^a, \tag{8}$$

with f_a the fraction of active updrafts at LCL. We find f_a by integrating the surface pdf over the light gray area of Fig. 2:

$$f_a = \frac{1}{2}\text{erfc}\left(\frac{\theta'_{v,\text{LFC}}}{\sqrt{2}\sigma_{\theta_v}}\right). \tag{9}$$

The mean velocity of the active updrafts at the LCL is

$$\overline{w_u(\text{LCL})}^a = \Gamma_{\theta_v}^{z_m}e^{2c_2\epsilon z_m}\frac{-2c_2 e^{-\epsilon(\text{LCL}-z_m+2c_2 z_m)} + 2c_2 e^{-2c_2\epsilon z_m} + e^{-2c_2\epsilon\text{LCL}} - e^{-2c_2\epsilon z_m}}{2c_2\epsilon(-e^{-2c_2\epsilon\text{LCL}} + e^{-\epsilon\text{LCL}})}. \tag{10}$$

Our formulation does not impose any a priori fraction of active updrafts [as in Siebesma et al. (2007); Neggers et al. (2009); Neggers (2009)]. The mass flux thus evolves as a function of the fractional coverage and vertical velocity of the active updrafts. Since the formulation has a similar flavor to Bretherton et al. (2004), to lowest order it defines a CIN criterion based on the vertical turbulent kinetic energy of the updrafts at LCL: initial buoyancy has to be sufficient to overcome the CIN imposed by the environmental profile and especially by the strength of the dry inversion $\Gamma_{\theta_v}^{z_m}$, as seen in Eq. (10).

4. Subcloud-layer evolution

a. Subcloud-layer growth

As in the clear-sky case, the energetic updrafts overshooting the dry inversion are responsible for the growth of h. The thermals reaching the dry inversion have to initially possess sufficient buoyancy $\theta_v' > \theta_{v,h}'$. The major differences with the dry case is that the updrafts with $\theta_v' > \theta_{v,\mathrm{LFC}}'$ overcome the CIN and leave the boundary layer, generating active convection. Those parcels reduce the growth of h since their mass flux is lost to the free troposphere (Stull 1985). The h growth is found using a mass budget [as in Stull (1985); Stevens (2006)]:

$$\frac{dh}{dt} = w_e - \frac{M_u^{\mathrm{active}}}{\rho} + \overline{w}. \tag{11}$$

The top-of-the-boundary-layer entrainment velocity in the absence of active convection is (Gentine et al. 2013)

$$w_e = \int_{\theta_{v,h}'}^{\infty} w_u(h) N(\theta_v') \, d\theta_v' = \frac{M_u(h)}{\rho}, \tag{12}$$

with $N(\theta_v')$ the surface Gaussian distribution in θ_v'. The updrafts participating in the growth of the boundary layer can be either dry or moist depending on whether the LCL is below or above h. In general, though the LCL is localized within the dry inversion layer and most thermals participating in the growth of the boundary layer are moist.

The mass flux of the active updrafts is also related to the surface pdf as

$$M_u^{\mathrm{active}} = \rho \int_{\theta_{v,\mathrm{LFC}}'}^{\infty} w_u(h) N(\theta_v') \, d\theta_v'. \tag{13}$$

Developing Eq. (11) in terms of the total updraft mass flux M_u gives

$$\rho \frac{dh}{dt} = M_u - M_u^{\mathrm{active}} + \rho \overline{w} = M_u^{\mathrm{nonactive}} + \rho \overline{w}. \tag{14}$$

The fundamental novelty of this new closure is that the active mass flux and entrainment velocity w_e are tightly coupled through the definition of the surface distribution and through the convective inhibition $\theta_{v,\mathrm{LFC}}'$. This buoyancy threshold is purely a diagnostic of the system depending on the evolving environmental profiles. Our new formulation thus extends the unified approach of Bretherton et al. (2004) since the entrainment velocity of the subcloud layer is also related to the mass flux of the (nonactive) updrafts. Our new formulation of the top of the boundary layer entrainment velocity naturally represents this smooth transition between dry and moist convection through a single formulation as will be demonstrated in the next section.

b. Mixed-layer growth

The mixed-layer top is diagnosed using the same formulation as in the dry case. We define the top of the mixed layer as the zero-buoyancy flux height [similar to Stull (1988) and Fedorovich et al. (2004)] and in order to find it, a single dry updraft is used as in Betts (1973). This updraft has properties averaged across all updrafts (i.e., $\theta_v' > 0$) and therefore has surface potential temperature and specific humidity anomalies of $\sigma_\theta/\sqrt{2\pi}$ and $\sigma_q/\sqrt{2\pi}$, respectively. The zero-buoyancy flux is diagnosed as the LNB of the updraft where $\theta_v^u(\mathrm{LNB}) = \theta_v^{\mathrm{env}}(\mathrm{LNB})$. Since lateral entrainment acts on the updraft throughout its rise in the boundary layer, this formulation of the mixed layer directly depends on ϵ.

The rate of growth of the mixed layer is found using the eddy overturning time scale $\tau = z_m/w_*$:

$$\frac{dz_m}{dt} = \frac{\mathrm{LNB} - z_m}{\tau} - \frac{M_u^{\mathrm{active}}}{\rho} + \overline{w}. \tag{15}$$

c. Mixed-layer heat budget

Using the Leibniz rule, the integration of the conservation equations for $\phi = \{\theta, q\}$ in the mixed layer yields [similar to Bretherton et al. (2004)]

$$z_m \frac{d\overline{\phi}}{dt} = \overline{w'\phi'}(0) + w_e \Delta\phi(z_m) - \frac{M_u^{\mathrm{active}}}{\rho}(\phi^u - \overline{\phi})$$
$$+ z_m \left(\frac{d\overline{\phi}}{dt}\right)_{\mathrm{LS}}, \tag{16}$$

with $\Delta\phi(z_m)$ the jump of ϕ at the mixed-layer top, obtained by extending the cloud layer profile to the mixed-layer top.

It should be noted that the active transport outside of the mixed-layer $M_u^{\text{active}}(\phi^u - \overline{\phi})$ is not accounted for in most bulk models of shallow convection (e.g., Albrecht et al. 1979; Stevens 2006; Bellon and Stevens 2005). This term reduces the moist static energy in the mixed layer and can be important when the surface heat fluxes are large. Our mixed-layer runs could not approach the large-eddy simulations outputs without inclusion of this moist static energy reduction term.

5. Cloud and moist inversion layers evolution

a. Cumulus layer growth

As mentioned, two diagnostic entraining plumes are used to define the growth rate and budget change of the cloud and inversion layers. The most energetic plume with anomaly $\theta_v' = 3\sigma_{\theta_v}$ is used to compute the cloud top. The plume trajectory, implied in our model, is depicted in Fig. 3.

The LNB of the bulk-diagnostic plume is used to define the rate of growth of z_1. The LNB of the bulk-diagnostic plume divides the lower layer (cloud layer) in which the effect of detrainment is relatively small from the upper layer (moist inversion layer) in which the updrafts are mainly negatively buoyant and the detrainment is the main process cooling and moistening the profile.

The rate of growth of z_1 is obtained from the diagnostic LNB:

$$\frac{dz_1}{dt} = \frac{\text{LNB} - z_1}{\tau}, \tag{17}$$

in which τ is the eddy overturning time scale approximated as (cloud top $-$ LCL)$/w_u(\text{LCL})$. This relaxation time scale is only used to ensure numerical stability in the growth of the cumulus layer. The scheme is almost insensitive to the definition of this time scale since the cloud layer evolution is rapid.

The top of the moist inversion layer is obtained from the diagnostic cloud top z_{top} of the $3\sigma_{\theta_v}$ plume, where its vertical velocity vanishes; that is, $w_u(z_{\text{top}}) = 0$:

$$\frac{dz_2}{dt} = \frac{z_{\text{top}} - z_2}{\tau}. \tag{18}$$

b. Cumulus heat and moisture budget

The evolution of the lapse rates of in the cloud layer can be found by writing the equation of conservation of temperature and humidity and averaging them over the layers (see the details of the derivation in appendix B; Emanuel 1994). In the moist inversion, between z_1 and z_2 this procedure gives

$$-\frac{(z_2 - z_1)^2}{2}\frac{d\Gamma_\theta^2}{dt} + (\gamma_\theta - \Gamma_\theta^2)(z_2 - z_1)\frac{dz_2}{dt}$$
$$= \overline{w'\theta_l'}(z_1) - \Gamma_\theta^2 \int_{z_1}^{z_2} \overline{w}(z)\,dz$$
$$+ R_{\text{tot}}(z_1) - R_{\text{tot}}(z_2), \quad \text{and} \tag{19}$$

$$-\frac{(z_2 - z_1)^2}{2}\frac{d\Gamma_q^2}{dt} + (\gamma_q - \Gamma_q^2)(z_2 - z_1)\frac{dz_2}{dt}$$
$$= \overline{w'q_{\text{tot}}'}(z_1) - \Gamma_q^2 \int_{z_1}^{z_2} \overline{w}(z)\,dz, \tag{20}$$

where $R_{\text{tot}}(z)$ is the total (cloud plus environment) radiative cooling rate at level z.

Analogously, in the cloud layer integration of the heat and moisture conservation equations between LCL and z_1 (see appendix B) gives the prognostic equations for Γ_θ^1 and Γ_q^1:

$$-\frac{(z_1 - \text{LCL})^2}{2}\frac{d\Gamma_\theta^1}{dt} - (z_1 - \text{LCL})(z_2 - z_1)\frac{d\Gamma_\theta^2}{dt} + (\gamma_\theta - \Gamma_\theta^2)(z_1 - \text{LCL})\text{LCL}\frac{dz_2}{dt} + (\Gamma_\theta^2 - \Gamma_\theta^1)(z_1 - \text{LCL})\frac{dz_1}{dt}$$
$$= \overline{w'\theta_l'}(\text{LCL}) - \overline{w'\theta_l'}(z_1) - \Gamma_\theta^1 \int_{\text{LCL}}^{z_1} \overline{w}(z)\,dz + R(\text{LCL}) - R(z_1), \quad \text{and} \tag{21}$$

$$-\frac{(z_1 - \text{LCL})^2}{2}\frac{d\Gamma_q^1}{dt} - (z_1 - \text{LCL})(z_2 - z_1)\frac{d\Gamma_q^2}{dt} + (\gamma_q - \Gamma_q^2)(z_1 - \text{LCL})\text{LCL}\frac{dz_2}{dt} + (\Gamma_q^2 - \Gamma_q^1)(z_1 - \text{LCL})\frac{dz_1}{dt}$$
$$= \overline{w'q_{\text{tot}}'}(\text{LCL}) - \overline{w'q_{\text{tot}}'}(z_1) - \Gamma_q^1 \int_{\text{LCL}}^{z_1} \overline{w}(z)\,dz. \tag{22}$$

To fully solve these equations, we need the turbulent transport terms $\overline{w'\theta_l'}$ and $\overline{w'q_{\text{tot}}}$ at two heights: LCL and z_1. These are found using the mass-flux equations described in section 3b above.

c. Method of solution

The model is integrated with a 1-min time step. In a model time step Δt, the growth of the different layers is
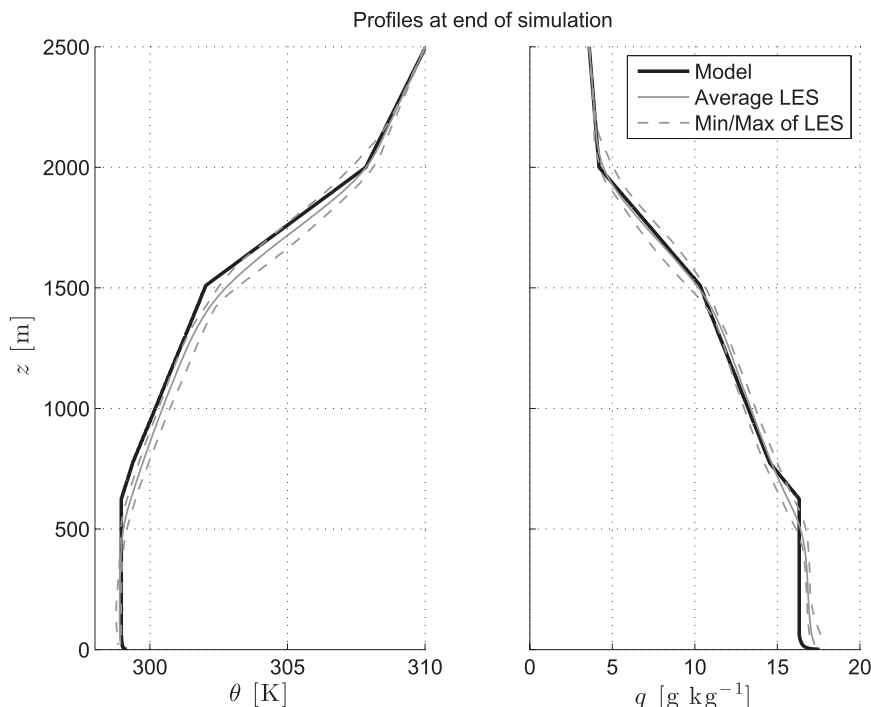
FIG. 4. Profiles of potential temperature and specific humidity obtained by PBCM (black line) and LES intercomparison results (continuous gray line represents the LES mean; minimum and maximum runs are depicted with dashed lines) at the end of the BOMEX run.

found using Eq. (15) for dz_m/dt, Eq. (11) for dh/dt, Eq. (17) for dz_1/dt, and Eq. (18) for dz_2/dt. These growth rates are then used to define the potential temperature and humidity changes in the mixed layer [Eq. (16)], cloud layer [Eqs. (21) and (22)] and moist inversion layer [Eqs. (19) and (20)]. The LCL is computed as the saturation level following a dry adiabatic using the mixed-layer potential temperature and specific humidity.

6. Comparison with observations and synthetic datasets

a. BOMEX

The LES intercomparison of steady-state trade wind cumulus from BOMEX (Siebesma et al. 2003) is used to evaluate PBCM. Figure 4 shows the PBCM profiles (thick line) compared to the mean, minimum, and maximum LES outputs at the end of the simulation (6 h). The surface and mixed-layer parameters are as in Gentine et al. (2013) for the clear-sky case. The PBCM correctly reproduces the temperature and humidity profiles. The steady-state cloud-base mass flux of the model is 0.025 kg m^{-1} s^{-1}, in good agreement with the mean LES value of 0.021 kg m^{-1} s^{-1}, and within the range of observed LES.

For nonprecipitating trade wind cumuli the rate of growth of the boundary layer in Eq. (14) is negligible. An equilibrium between entrainment, convection, and subsidence is created in the subcloud layer (Stevens 2006); namely,

$$w_e - \frac{M_u^{\text{active}}}{\rho} + \overline{w} = \frac{M_u^{\text{nonactive}}}{\rho} + \overline{w} = 0. \qquad (23)$$

In typical shallow convection parameterization the entrainment velocity and active mass flux are imposed through separate parameterizations. As discussed in section 4, our formulation couples the entrainment velocity and active mass flux through CIN, with the latter acting as a valve that reduces the growth and moist static energy of the mixed layer (Betts 1970, 1973). The inhibition at steady state is directly related to the magnitude of the subsidence. We believe that our formulation of this balance in terms of the surface-layer probability distribution gives fundamental new understanding into the subcloud layer equilibrium of nonprecipitating shallow convection. In addition, the cloud cover responds naturally to this coupling through the definition of $\theta_{v,\text{LCL}}$, which depends on the same buoyancy distribution and on the mixed-layer state LCL$(\overline{\theta})$. Of course, the characteristics of the cloud cover also depend on

microphysics, which is not considered in this specific study.

The cumulus layer is in radiative–convective equilibrium. Summing Eqs. (19) and (21) at steady state depicts the following radiative–convective equilibrium:

$$\Gamma_\theta^1 \int_{\text{LCL}}^{z_1} \overline{w}(z)\, dz + \Gamma_\theta^2 \int_{z_1}^{z_2} \overline{w}(z)\, dz = R_{\text{tot}}(\text{LCL}) - R_{\text{tot}}(z_2),$$
(24)

where $\overline{w'\theta_l'}(\text{LCL})$ is neglected since surface sensible heat flux is small in the trade wind case (Betts 1974, 1975).

Equation (24) demonstrates the strong coupling between the temperature stratification of the cloud and moist inversion layers (Betts 1973). Radiative cooling compensates the warming through subsidence (Betts and Ridgway 1989; Emanuel 1994). The microphysics alters the radiation in Eq. (24) and the cumulus temperature lapse rates by adjustment.

Similarly, in terms of humidity, a convective–moisture flux equilibrium is created. Summing Eqs. (20) and (22) at steady state,

$$\Gamma_q^1 \int_{\text{LCL}}^{z_1} \overline{w}(z)\, dz + \Gamma_q^2 \int_{z_1}^{z_2} \overline{w}(z)\, dz = \overline{w'q'}(\text{LCL}).$$
(25)

The cloud-base latent heat flux compensates for the drying induced by subsidence. Using the mixed-layer equilibrium budget for moisture in Eq. (16), neglecting the moisture flux divergence in the mixed layer, which is small at equilibrium, and integrating the moisture budget between the surface and z_2 yields

$$\Gamma_q^1 \int_{\text{LCL}}^{z_1} \overline{w}(z)\, dz + \Gamma_q^2 \int_{z_1}^{z_2} \overline{w}(z)\, dz \approx \overline{w'q'}(0)$$
(26)

to the first order. Consequently, if surface latent heat flux increases (i.e., sea surface temperature warming), nonprecipitating trade wind cumuli deepen, under similar large-scale subsidence conditions, until they reach a deep convective regime.

b. ARM SGP 21 June 1997

The SGP Cloud and Radiation Testbed (CART) is operated by the U.S. Department of Energy as part of ARM. Results of the PBCM are tested using data from 21 June 1997, which is a reference case of shallow convection over land (Brown et al. 2002). This day was selected since negligible large-scale advection and convergence forcing were present. We use the same forcing as in the LES: no large-scale divergence $\overline{w} = 0$ and negligible radiative cooling $R_{\text{tot}} = 0$, since most of the dynamics was supposed to be imposed by the surface forcing.

Instead of using direct observations, the synthetic forcing imposed in the LES is used (Brown et al. 2002). This synthetic experiment facilitates the intercomparison among models and reduces the observed variability in the atmospheric sounding. A piecewise-linear temporal forcing of the surface heat fluxes was imposed as shown in Fig. 5. The initial atmospheric profiles are also the same as the ones imposed in the LES intercomparison and are depicted in Fig. 5.

The simulation is run from 1130 UTC 21 June until 0200 UTC 22 June and compared to the output of a LES performed with the same forcing using the Dutch Atmospheric Large-Eddy Simulation (DALES) model (Heus et al. 2010).

c. Boundary layer heights

The heights of the PBCM are compared with the outputs of the LES. Figure 6 shows z_m, LCL, z_2, and z_{top}.

The timing of the appearance of forced cloud cover (1500 UTC) is perfectly captured by the PBCM compared to the LES outputs. The timing of the active convection triggering is also perfectly captured by the model, as emphasized by the mass flux at cloud base depicted in Fig. 7. The diurnal course of the cloud-base and cloud-top heights is also satisfying.

d. Mass flux and lapse rates

The mass flux of the PBCM compares well with the LES, as seen in Fig. 7, although PBCM slightly overestimates the value relative to LES. That the mass flux at cloud base is well represented by the PBCM both in terms of timing of the mass-flux triggering as well as of magnitude further confirms the realism of the simplifications and physical assumptions of the model.

The profiles of the model are depicted in Figs. 8 and 9. The dynamics of the atmospheric profiles and of the mixed layer are well captured by the PBCM, further confirming the importance of the coupling between the subcloud and cumulus layers. These results are especially encouraging since no tuning has been performed on the model parameters. Before 2030 UTC no active cumulus is present and all of the cloud cover is forced, as the CIN has not been overcome. Once the first active cloud emerges, the layer above the dry inversion (cloud layer) moistens and becomes more conditionally unstable further facilitating the rise of subsequent updrafts.

e. Cloud cover

The cloud cover of the PBCM is compared to outputs from the LES intercomparison of Brown et al. (2002) in Fig. 10. Forced cloud cover is obtained as the fraction of plumes with $\theta_{v,\text{LCL}}' < \theta_v' < \theta_{v,\text{LFC}}'$. Active cloud cover is due to the active updrafts with $\theta_v' > \theta_{v,\text{LFC}}'$. The total
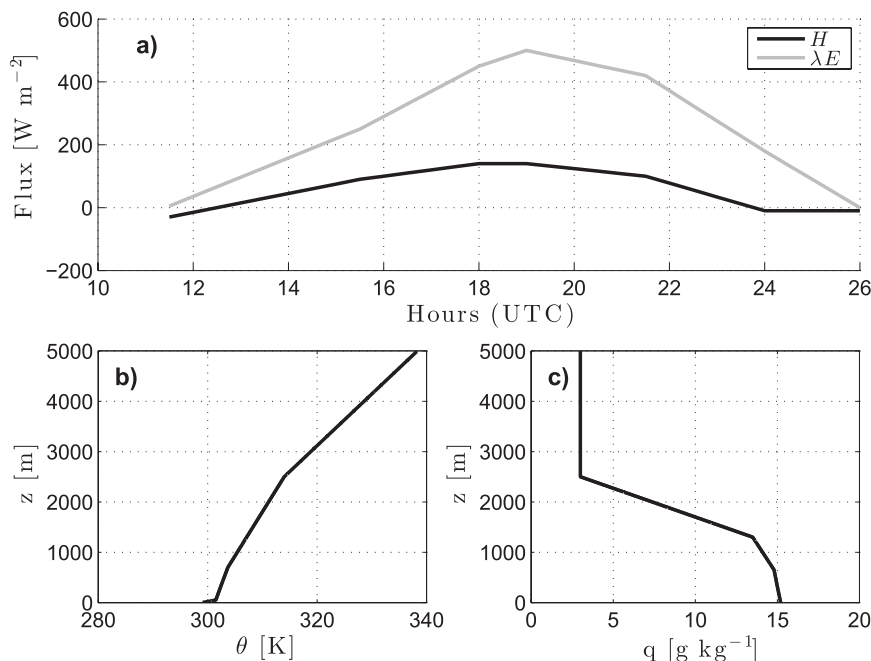
FIG. 5. (a) Turbulent heat flux forcing and (b),(c) initial atmospheric profiles as imposed in the large-eddy simulation intercomparison of 21 Jun 1997 for ARM SGP site in Oklahoma (Brown et al. 2002).

cloud cover is the sum of the forced and active cloud cover. The model is run at a 30-min time step, which corresponds to the typical life time of a convective cloudy updraft. We have no explicit model for passive or decaying clouds.

There is substantial spread of the cloud cover between the different LES outputs. In the earlier stage of the cloud cover occurrence the PBCM tends to underestimate the total cloud cover. The PBCM active cloud cover is able to reproduce the decay of the cloud cover later in the day. This evolution of the active cloud cover reflects the increase of the CIN through the reduced surface buoyancy anomalies of the parcels. The forced cloud cover tends to be overestimated in the late afternoon (after 2200 UTC). The higher forced cloud cover can point to a possible underestimation of the LCL in the PBCM compared to LES: this effect is evident in the humidity profiles at 2130 UTC, as the PBCM is moister than the LES.
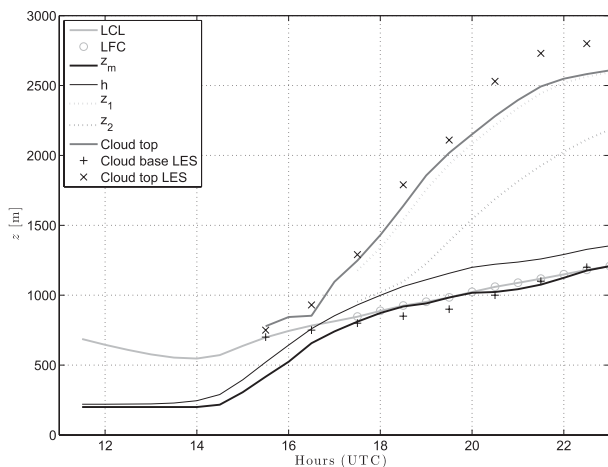

FIG. 6. PBCM levels evolution as a function of time of day, compared with cloud base and top from large-eddy simulations of 21 Jun 1997 for ARM SGP site in Oklahoma. Cumulus-related PBCM levels are only plotted when active convection is triggered.
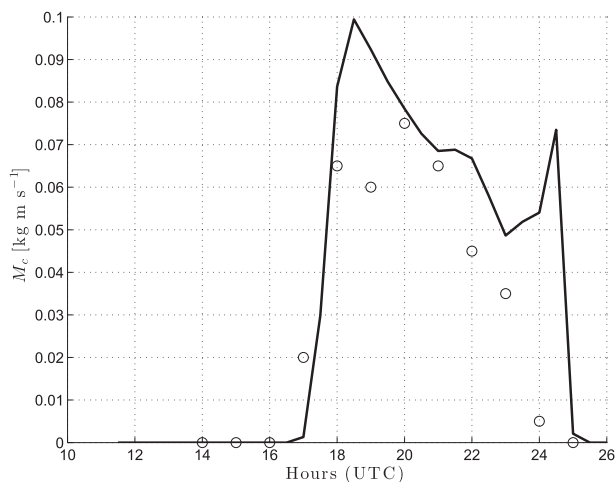

FIG. 7. Comparison of PBCM mass flux at the LCL compared to large-eddy simulations of 21 Jun 1997 for ARM SGP site in Oklahoma. Black continuous line represents the PBCM outputs and the circles represent the results from LES.
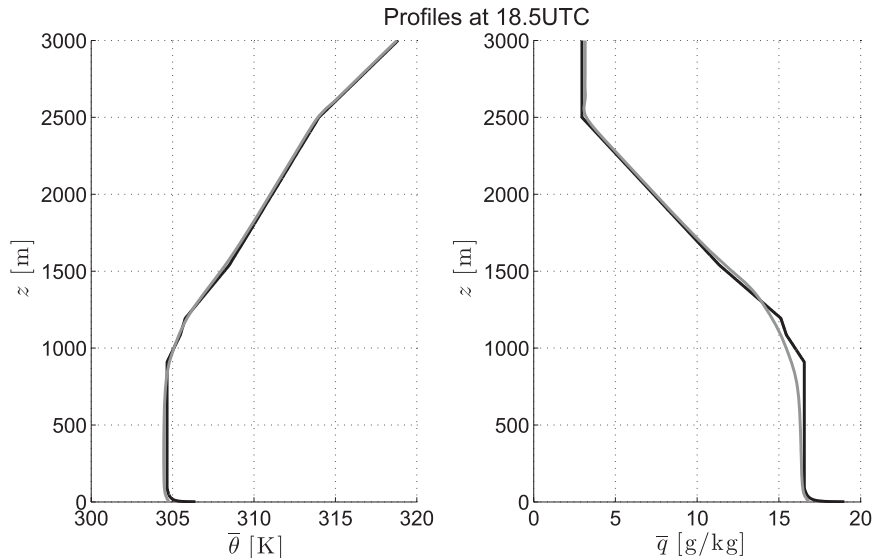
FIG. 8. Potential temperature and specific humidity profiles at 1830 UTC for the 21 Jun 1997 ARM SGP case. PBCM is black; LES is gray.

f. Mixed-layer entrainment

The diurnal course of the LCL, which is both a cause and consequence of the mixed-layer growth, exhibits a tight coupling with the mixed-layer growth z_m. When the mixed-layer top approaches the LCL the mixed-layer growth is reduced because of the active mass flux of updrafts leaving the subcloud layer. An equilibrium is reached in which $z_m \approx$ LCL and $d\text{LCL}/dt = w_e^{\text{nonactive}} - M_u^{\text{active}}/\rho + \overline{w}$. The LCL rise, induced by dry, warm air entrainment from the cloud layer into the mixed layer, defines the growth of the mixed layer since z_m and LCL are tied together. The CIN $\theta'_{v,\text{LFC}}$ controls both the mixed-layer growth and the active mass flux at cloud base. Our modeling of this coupling is a fundamental improvement in the description of the feedback between the mixed layer and shallow convection.

7. Sensitivity

Here, we test the sensitivity of the PBCM by modifying the main parameters of the mixed layer and convection models for the ARM case. We increase the surface variance [var(θ) and var(q)], the coefficient of lateral entrainment c_e, and the parameters of the plume model c_1, c_2 by 10% and 100% as shown in Table 2. In section 7d we discuss the sensitivity to the detrainment formulation.

a. Variability at the surface

A 10% increase in the variance of θ leads to almost no changes in the mixed-layer, cloud, and moist-inversion-layer tops. The main reason for the lack of change in the evolution of the different layers is that the dry inversion layer, which controls the CIN, adjusts to the kinetic energy of the updrafts. Its strength also controls the dry CIN and therefore the entrainment velocity of the subcloud layer. This tight coupling leads to reduced modification of the dynamics when modifying the surface variance and thus confirms the stability of the model as it is rather insensitive to the exact definition of the parameters. The effect of the variance of the surface potential temperature is more readily observed on the cloud and inversion lapse rates. Both the temperature and humidity lapse rates are affected. The moist inversion layer is drier and warmer. The higher liquid potential temperature variance leads to increased enthalpy flux at the moist inversion base $\overline{w'\theta_l}(z_1) = M_u(z_1)[\theta_l^u(z_1) - \overline{\theta}(z_1)] < 0$. As a consequence the partitioning of heat in the cumulus (cloud plus moist inversion) favors heating in the cloud layer. Since the surface humidity variance has not been modified, the updrafts have higher potential temperature for the same humidity amount. That is, each updraft carries a humidity deficit compared to the reference case. Consequently, the latent heat flux at the moist inversion base is reduced and the moist inversion dries up. An increase in the variance of specific humidity, var(q) has a very small impact on the overall structure.

The 100% increase in the surface temperature variance, shown in the lower section of Table 2, is a more demanding test of the model sensitivity. This mostly impacts the cloud-base mass flux, which increases by 19%, and the slope of the potential temperature in the moist inversion, which increases by 29%. The mixed-layer depth increases by about 10%. The other variables do
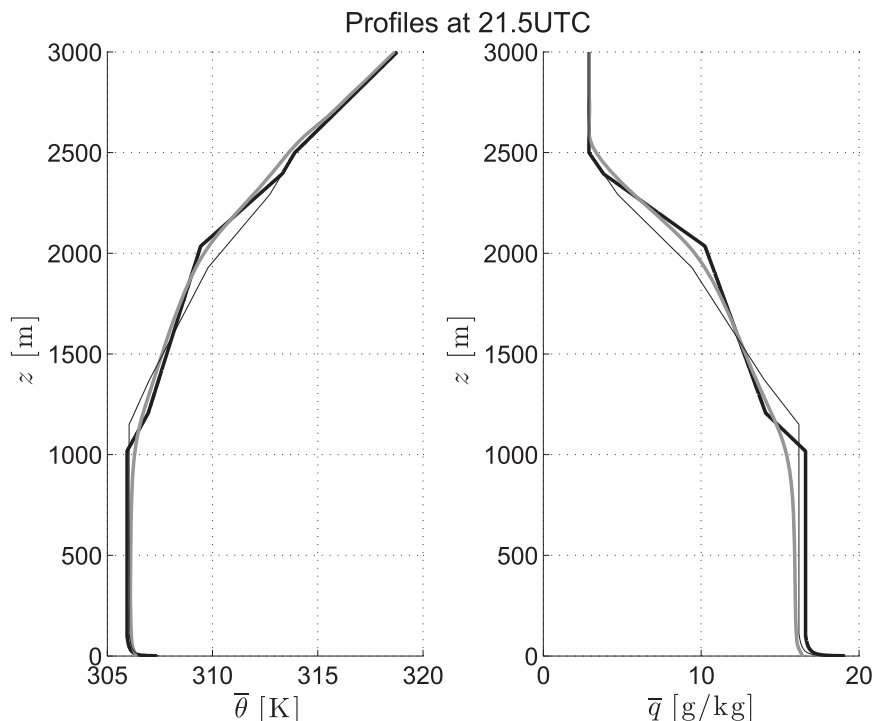
FIG. 9. Potential temperature and specific humidity profiles at 2130 UTC for the 21 Jun 1997 ARM SGP case. PBCM is thick black, LES is thick gray, and the constant detrainment $\delta = 2 \times 10^{-3}$ m^{-1} case is thin black.

not change more than 5%. Doubling the specific humidity variance induces a 13% increase in the cloud-layer moisture slope and reduces the moist inversion slope by 12%. This corresponds to a strong moistening of the cloud layer produced by the moister updrafts.

b. Plume model

In the plume model, c_1 controls the efficiency of the transformation of buoyancy into vertical turbulent kinetic energy and c_2 corresponds to a drag term induced by the mixing with the environment.

Surprisingly, a 10% increase in c_1 has almost no effect on the height of the cloud and inversion levels. The mixed-layer top decreases with c_2 since the updrafts are less energetic. The cloud-base mass flux is reduced in this reduced-magnitude sensitivity test. A possible explanation is the deepening of the dry inversion layer, which reduces the cloud-base mass flux and therefore increase of the CIN. The lapse rates of the cloud and moist inversion layer are noticeably affected by the change in the buoyancy efficiency and drag coefficient. This is rather obvious since those changes induce a modification of the partitioning of the turbulent transport between the cloud and moist inversion layers. A rise in c_1 increases all lapse rates except the inversion-layer humidity lapse rate. Increasing the plume drag has an opposite effect. Overall

the sensitivity responses (maximum of 6.2% variation) are smaller than the initial perturbation of 10%.

With a 100% increase in c_1, the kinetic energy acquired through buoyancy in the mixed layer becomes large. As a consequence, the mass flux at cloud base experiences a large increase of 43%. The moist inversion is much
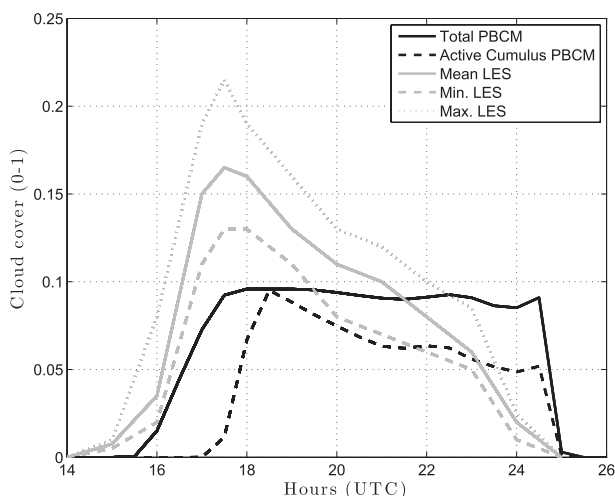

FIG. 10. PBCM total (continuous black line) and active cloud cover (dashed black line) compared to the mean (continuous gray line), minimum (dashed gray line), and maximum (dotted gray lines) LES outputs of Brown et al. (2002).

TABLE 2. Sensitivity study: daylight-hours average of a change of variable Y, $\Delta Y/Y$, for a change ΔX equal of initial reference value X: $\Delta X/X = 10\%$ and 100%. All values are percentages.

	$Y = \Gamma_\theta^1$	$Y = \Gamma_\theta^2$	$Y = \Gamma_q^1$	$Y = \Gamma_q^2$	$Y = M_c$	$Y = z_m$	$Y = z_1$	$Y = z_2$
				$\Delta Y/Y$ for $\Delta X/X = 10\%$				
var(θ)	−0.8	3	2.8	−0.9	−2.8	0.9	0.3	0.7
var(q)	−0.2	1.1	2.2	−1.6	−2.9	0.1	0.2	0.4
c_1	0.4	4.4	6.2	−2.5	−4.3	0.5	0.4	1.3
c_2	−0.5	−3.7	−5.6	1.4	0.2	−2.7	−1.1	−2.1
c_s	−5.1	−1.4	−9.5	4.6	2.4	−2.9	−3.3	−4.5
				$\Delta Y/Y$ for $\Delta X/X = 100\%$				
var(θ)	−5	29.1	1.6	−1.3	18.6	9.3	2	5.8
var(q)	1.3	8.9	12.6	−11.6	−6.4	1.5	1.1	3
c_1	4.4	38.5	2.8	−1.8	43.2	6.1	2.1	8.6
c_2	−5.8	−6.3	−12.1	1.8	−28.4	−10.6	−10.1	−12
c_ϵ	8.7	10.3	14.8	25.9	−22.3	−3.5	−27.7	−21.9

warmer with an increase of the 39% of the slope. The other changes are small. When doubling c_2, the drag increases and the mass flux at cloud base is reduced by 28%. The mixed-layer, cloud-, and moist-inversion-layer tops are subsequently reduced by about 10%.

c. Entrainment

A 10% increase in c_ϵ gives a small increase in cloud-base mass flux. The mixed-layer height is reduced by 3%, z_1 by 3%, and z_2 by 5%. Doubling the entrainment rate leads to a strong decrease in the cloud-layer top (28%) and in the moist-inversion-layer top (22%). The mixed-layer depth only exhibit small changes (−3%) similar to the 10% sensitivity test. With the larger rise in entrainment rate, the mass flux strongly decreases (22%), which is a more intuitive result than in the small-increase case. The humidity in the moist inversion is strongly reduced: the moist-inversion specific humidity lapse rate increases by 26%. The lateral mixing with the environment reduces the moisture of the air reaching the moist inversion yet it also affects the depth of the cumulus layer. Overall, the increased entrainment dries out the cumulus layer but the specific humidity slopes are steeper because of the reduced cumulus depth.

d. Detrainment and mass-flux formulation

We compared our reference detrainment scheme to a constant and uniform detrainment rate, $\delta = 3 \times 10^{-3}$ m^{-1} (Bechtold and Siebesma 1998; Soares et al. 2004), in order to evaluate the role of detrainment on the cloud and mixed-layer dynamics. The constant detrainment is insufficient to maintain a cool and moist inversion layer as seen in Fig. 9. This weak moist inversion directly impacts the diurnal dynamics of the cloud top, which becomes lower than with the reference detrainment scheme as seen in Fig. 11. Insufficient detrainment occurs in the moist inversion layer, and as a consequence the cloud

layer is too stable. The plume entrains drier air in the upper cloud layer, reducing its buoyancy. The cloud top is then reduced.

This sensitivity test emphasizes the fundamental role of detrainment on both the dynamics and thermodynamics of shallow convection (Betts 1975). In the model, the detrainment rate is the most sensitive parameter, and it affects the mass flux at z_1. A modification of the mass flux at z_1 adjusts the partitioning of the heat and moisture transport between the cloud and moist inversion layers.

We use the BOMEX case to evaluate the effect of the detrainment on the transient and steady-state mass-flux response (Fig. 12). During the transient part of the run (first few hours), the scheme of de Rooy and Siebesma (2008) exhibits a much higher mass flux at z_1 than the constant detrainment case. As a result, realistic temperature and humidity structures are obtained, with a stronger moister inversion. At the end of the run, both simulations have comparable mass flux $M_u(z_1)$ since the heat flux at
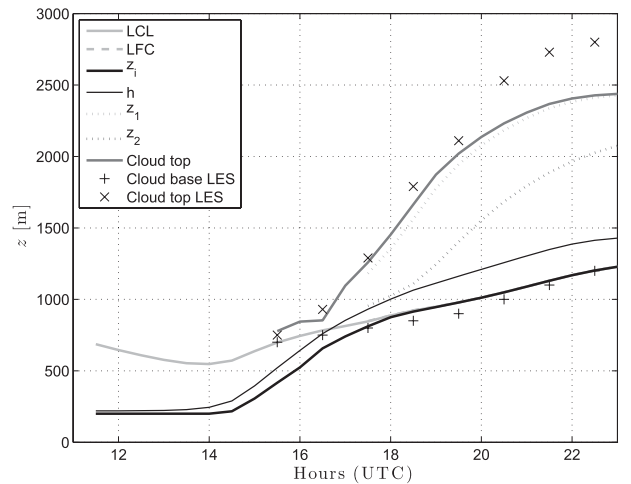

FIG. 11. As in Fig. 6, but using the constant detrainment $\delta = 2 \times 10^{-3}$ m^{-1} formulation.
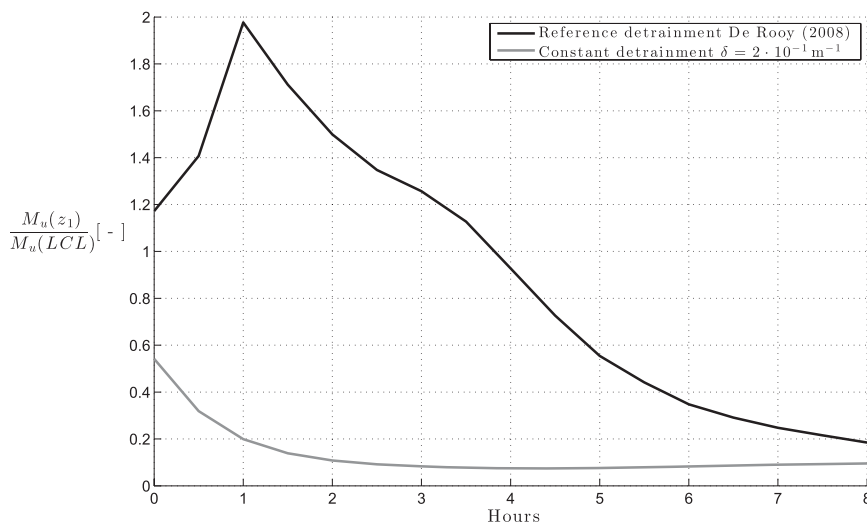
FIG. 12. Comparison of the updraft mass flux in z_1 compared to the LCL value in the BOMEX case using the formulation of de Rooy and Siebesma (2008) and the constant detrainment $\delta = 2 \times 10^{-3}$ m^{-1} formulation.

the inversion base has to adjust to respect the radiative–convective equilibrium since radiation is imposed in these runs. Interactive radiation may impact the steady-state equilibrium.

These results show that a strong coupling exists between the moist static energy of the cloud layer, its stability, the moist inversion to cloud-top depth and the mass flux at the base of the moist inversion. A moist, more unstable, cloud layer favors higher penetration of the updrafts because of the reduced entrainment. The moist inversion becomes sharper and the relative depth of the cloud layer to the total cloud depth $(z_1 - \text{LCL})/(z_{\text{top}} - \text{LCL})$ increases. In turn, the detrainment in the cloud layer is reduced, as captured by the scheme of de Rooy and Siebesma (2008), and as a result, the cloud depth increases. The detrainment and entrainment rates are thus strongly coupled via the height of the moist inversion. It is this coupling that imposes the exact partitioning of heat between the cloud and moist inversion layers and the dynamics of the shallow convection. The detrainment and entrainment rates should thus not be thought of as independent parameters. Buoyancy-sorting algorithms take into account some of this coupling (Raymond and Blyth 1986; Kain and Fritsch 1990; Emanuel 1991; Bretherton et al. 2004), as opposed to constant detrainment schemes. Further work is required to understand the coupling of these two processes.

8. Conclusions

A new bulk model of the coupled mixed layer and shallow convection, the probabilistic bulk coupled model (PBCM), is developed. The PBCM is able to represent a smooth transition between dry and moist convection.

Shallow convection is divided into forced convection, thermals emerging from the dry boundary layer reaching their condensation level but not their level of free convection, and active convection, with positively buoyant updrafts having reached both their LCL and LFC.

The PBCM has several advantages over previous approaches:

- The mass flux at cloud base is directly related to the fraction of "active" updrafts able to reach the level of free convection (LFC) by overcoming the convective inhibition (CIN) and to their vertical kinetic energy at the lifting condensation level (LCL).
- The mixed-layer entrainment is expressed as the mass flux of the nonactive thermals able to overshoot the inversion. Our formulation unifies the treatment of the mixed-layer growth and cloud-base mass flux, introducing an important coupling for the mixed-layer state and dynamics.
- The cloud cover is naturally represented in the model through the definition of a buoyancy threshold $\theta'_{v,\text{LCL}}$ for the updrafts originating from the surface. This potentially allows the modeling of the coupling between the radiation (with the addition of a microphysics scheme) and the convective mass flux.

We have demonstrated that accurate detrainment in the moist inversion layer strongly controls the structure and dynamics of the cumulus (cloud plus inversion) layer. Inaccuracies in the detrainment process lead to incorrect heat and moisture stratification and dynamics of the

cloud and inversion layers. Further research about the detrainment process is needed [as highlighted by de Rooy and Siebesma (2008) and de Rooy et al. (2013)] to accurately describe the temperature and moisture profiles of shallow convection and transition from shallow to deep convection. It is shown that the definition of the mass flux at the base of the inversion imposes the heat and moisture transport partitioning between the cloud and inversion layers. The detrainment and entrainment rates need to be considered as dependent parameters. The PBCM is currently being extended to account for nonsurface generated sources of turbulence such as cold pools, which is important for the transition and duration of deep convection, and radiatively driven turbulence, which is a fundamental mechanism of TKE generation in the stratocumulus-topped boundary layer.

APPENDIX A

Derivation of Moist Adiabatic Lapse Rates

The moist adiabatic lapse rate of the updrafts is derived as follows. First, a hydrostatic approximation is used to find the pressure dependence in vertical coordinates:

$$P(z) = P_0 \left(1 - \frac{gz}{C_p \overline{\theta}} \right)^{C_p/R_d}. \tag{A1}$$

The liquid temperature is defined from the liquid potential temperature:

$$T_l = \theta_l \left(\frac{P}{P_0} \right)^{R_d/C_p}. \tag{A2}$$

The saturation specific humidity is linearized around the liquid temperature in order to calculate the first guess of the liquid temperature:

$$q_{\text{sat}} = qs_{T_l} + dqs_{T_l}(T - T_l), \tag{A3}$$

with

$$qs_{T_l} = q_{\text{sat}}(T_l, P) \quad \text{and} \tag{A4}$$

$$dqs_{T_l} = \frac{\partial q_{\text{sat}}}{\partial T}(T_l, P). \tag{A5}$$

This linearized saturation value is used to determine the liquid specific humidity since the total humidity $q_{\text{tot}} = q_{\text{sat}} + q_l$ is conserved (neglecting supersaturation):

$$q_l = \max \left[\frac{q_{\text{tot}} - qs_{T_l}}{1 + (\lambda/C_p)dqs_{T_l}}, 0 \right]. \tag{A6}$$

The potential temperature is then found from its relationship with the liquid potential temperature and liquid specific humidity:

$$\theta = \theta_l + \frac{\lambda}{C_p} q_l. \tag{A7}$$

The absolute temperature is then found as

$$T = \theta \left(\frac{P}{P_0} \right)^{R_d/C_p}. \tag{A8}$$

APPENDIX B

Derivation of Conservation Equations in the Cloud and Inversion Layer

The conservation equation for the averaged liquid potential temperature reads

$$\frac{\partial \overline{\theta_l}}{\partial t} = -\frac{\partial \overline{w'\theta_l'}}{\partial z} - \overline{w}\frac{\partial \overline{\theta_l}}{\partial z} - \frac{\partial R_{\text{tot}}}{\partial z}, \tag{B1}$$

where R_{tot} represents the total radiative flux (cloud plus environment) per unit height, and $\overline{X}$ represents the areal mean of X at level z.

For humidity,

$$\frac{\partial \overline{q_{\text{tot}}}}{\partial t} = -\frac{\partial \overline{w'q_{\text{tot}}'}}{\partial z} - \overline{w}\frac{\partial \overline{q_{\text{tot}}}}{\partial z} - P, \tag{B2}$$

where P is the precipitation per unit height.

The areal-average liquid potential temperature can be divided into two terms: $\overline{\theta_l} = \overline{\theta} - (\lambda/C_p)\overline{q_l}$. Similarly, $\overline{q_{\text{tot}}} = \overline{q} + \overline{q_l}$. The liquid water content is only present in the cloudy region. This latter term is negligible during

the active convection regime since the cloud cover is very small. Consequently, $\overline{\theta_l} \approx \overline{\theta}$ and $\overline{q_{\text{tot}}} \approx \overline{q}$.

We can thus rewrite the conservation equations in terms of $\overline{\theta}$ and $\overline{q}$, which will be integrated to obtain the lapse-rate evolution:

$$\frac{\partial \overline{\theta}}{\partial t} = -\frac{\partial \overline{w'\theta_l'}}{\partial z} - \overline{w}\frac{\partial \overline{\theta}}{\partial z} - \frac{\partial R_{\text{tot}}}{\partial z}, \qquad (\text{B3})$$

$$\frac{\partial \overline{q}}{\partial t} = -\frac{\partial \overline{w'q_{\text{tot}}'}}{\partial z} - \overline{w}\frac{\partial \overline{q_{\text{tot}}}}{\partial z} - P, \qquad (\text{B4})$$

We here consider the case of nonprecipitating cumulus. The heat flux on top of the cloud is assumed negligible.

This latter equation can be integrated between LCL and z_1:

$$-\frac{(z_1 - \text{LCL})^2}{2}\frac{d\Gamma_\theta^1}{dt} - (z_1 - \text{LCL})(z_2 - z_1)\frac{d\Gamma_\theta^2}{dt} + (\gamma_\theta - \Gamma_\theta^2)(z_1 - \text{LCL})\frac{dz_2}{dt} + (\Gamma_\theta^2 - \Gamma_\theta^1)(z_1 - \text{LCL})\frac{dz_1}{dt}$$
$$= \overline{w'\theta_l'}(\text{LCL}) - \overline{w'\theta_l'}(z_1) - \Gamma_\theta^1 \int_{\text{LCL}}^{z_1} \overline{w}(z)\,dz + R_{\text{tot}}(\text{LCL}) - R_{\text{tot}}(z_1). \qquad (\text{B5})$$

Similarly, between z_1 and z_2,

$$-\frac{(z_2 - z_1)^2}{2}\frac{d\Gamma_\theta^2}{dt} + (\gamma_\theta - \Gamma_\theta^2)(z_2 - z_1)\frac{dz_2}{dt} = \overline{w'\theta_l'}(z_1) - \Gamma_\theta^2 \int_{z_1}^{z_2} \overline{w}(z)\,dz + R_{\text{tot}}(z_1) - R_{\text{tot}}(z_2). \qquad (\text{B6})$$

For humidity, similar equations are obtained:

$$-\frac{(z_1 - \text{LCL})^2}{2}\frac{d\Gamma_q^1}{dt} - (z_1 - \text{LCL})(z_2 - z_1)\frac{d\Gamma_q^2}{dt} + (\gamma_q - \Gamma_q^2)(z_1 - \text{LCL})\frac{dz_2}{dt} + (\Gamma_q^2 - \Gamma_q^1)(z_1 - \text{LCL})\frac{dz_1}{dt}$$
$$= \overline{w'q_{\text{tot}}'}(\text{LCL}) - \overline{w'q_{\text{tot}}'}(z_1) - \Gamma_q^1 \int_{\text{LCL}}^{z_1} \overline{w}(z)\,dz. \qquad (\text{B7})$$

Similarly, between z_1 and z_2,

$$-\frac{(z_2 - z_1)^2}{2}\frac{d\Gamma_q^2}{dt} + (\gamma_q - \Gamma_q^2)(z_2 - z_1)\frac{dz_2}{dt} = \overline{w'q_{\text{tot}}'}(z_1) - \Gamma_q^2 \int_{z_1}^{z_2} \overline{w}(z)\,dz. \qquad (\text{B8})$$

The turbulent heat transport terms are described in section 5.

REFERENCES

Albrecht, B., 1984: A model study of downstream variations of the thermodynamic structures of the trade winds. *Tellus,* **36A,** 187–202.

——, A. K. Betts, W. Schubert, and S. Cox, 1979: Model of the thermodynamic structure of the trade-wind boundary layer: Part I. Theoretical formulation and sensitivity tests. *J. Atmos. Sci.,* **36,** 73–89.

Arakawa, A., and W. Schubert, 1974: Interaction of a cumulus cloud ensemble with the large-scale environment, Part I. *J. Atmos. Sci.,* **31,** 674–701.

Bechtold, P., and A. P. Siebesma, 1998: Organization and representation of boundary layer clouds. *J. Atmos. Sci.,* **55,** 888–895.

Beljaars, A. C. M., and A. A. M. Holtslag, 1991: Flux parameterization over land surfaces for atmospheric models. *J. Appl. Meteor.,* **30,** 327–341.

Bellon, G., and B. Stevens, 2005: On bulk models of shallow cumulus convection. *J. Atmos. Sci.,* **62,** 3286–3302.

Berg, L., and R. B. Stull, 2004: Parameterization of joint frequency distributions of potential temperature and water vapor mixing ratio in the daytime convective boundary layer. *J. Atmos. Sci.,* **61,** 813–828.

Betts, A. K., 1970: Cumulus convection. Ph.D. dissertation, University of London, 151 pp. [Available online at http://alanbetts.com/research/paper/cumulus-convection/.]

——, 1973: Non-precipitating cumulus convection and its parameterization. *Quart. J. Roy. Meteor. Soc.,* **99,** 178–196.

——, 1974: Scientific basis and objectives of U.S. convection subprogram for the GATE. *Bull. Amer. Meteor. Soc.,* **55,** 304–313.

——, 1975: Parametric interpretation of trade-wind cumulus budget studies. *J. Atmos. Sci.,* **32,** 1934–1945.

——, 1985: Mixing-line analysis of clouds and cloudy boundary layers. *J. Atmos. Sci.,* **42,** 2751–2763.

——, 1986: A new convective adjustment scheme. Part I: Observational and theoretical basis. *Quart. J. Roy. Meteor. Soc.,* **112,** 677–691.

——, and M. J. Miller, 1986: A new convective adjustment scheme. Part II: Single column tests using GATE wave, BOMEX, ATEX and Arctic air-mass data-sets. *Quart. J. Roy. Meteor. Soc.,* **112,** 693–709.

——, and W. Ridgway, 1989: Climatic equilibrium of the atmospheric convective boundary layer over a tropical ocean. *J. Atmos. Sci.,* **46,** 2621–2641.

Bony, S., and K. A. Emanuel, 2001: A parameterization of the cloudiness associated with cumulus convection:

Evaluation using TOGA COARE data. *J. Atmos. Sci.,* **58,** 3158–3183.

——, and Coauthors, 2006: How well do we understand and evaluate climate change feedback processes? *J. Climate,* **19,** 3445–3482.

Bretherton, C. S., and S. Park, 2008: A new bulk shallow-cumulus model and implications for penetrative entrainment feedback on updraft buoyancy. *J. Atmos. Sci.,* **65,** 2174–2193.

——, and ——, 2009: A new moist turbulence parameterization in the Community Atmosphere Model. *J. Climate,* **22,** 3422–3448.

——, J. R. McCaa, and H. Grenier, 2004: A new parameterization for shallow cumulus convection and its application to marine subtropical cloud-topped boundary layers. Part I: Description and 1D results. *Mon. Wea. Rev.,* **132,** 864–882.

Brocks, K., E. Augstein, and L. Krugerme, 1970: Turbulent vertical fluxes in planetary boundary layer and their relation to synoptic-scale processes during the Atlantic Trade Wind Experiment 1969 (ATEX). *Bull. Amer. Meteor. Soc.,* **51,** 287–289.

Brown, A., and Coauthors, 2002: Large-eddy simulation of the diurnal cycle of shallow cumulus convection overland. *Quart. J. Roy. Meteor. Soc.,* **128,** 1075–1093.

Cheinet, S., 2003: A multiple mass-flux parameterization for the surface-generated convection. Part I: Dry plumes. *J. Atmos. Sci.,* **60,** 2313–2327.

——, 2004: A multiple mass-flux parameterization for the surface-generated convection. Part II: Cloudy cores. *J. Atmos. Sci.,* **61,** 1093–1113.

De Bruin, H., B. van den Hurk, and L. Kroon, 1999: On the temperature-humidity correlation and similarity. *Bound.-Layer Meteor.,* **93,** 453–468.

de Rooy, W. C., and P. Siebesma, 2008: A simple parameterization for detrainment in shallow cumulus. *Mon. Wea. Rev.,* **136,** 560–576.

——, and Coauthors, 2013: Entrainment and detrainment in cumulus convection: An overview. *Quart. J. Roy. Meteor. Soc.,* **139,** 1–19.

Donohoe, A., and D. Battisti, 2012: What determines meridional heat transport in climate models? *J. Climate,* **25,** 3832–3850.

Emanuel, K. A., 1991: A scheme for representing cumulus convection in large-scale models. *J. Atmos. Sci.,* **48,** 2313–2335.

——, 1994: *Atmospheric Convection.* Oxford University Press, 580 pp.

Fedorovich, E., R. Conzemius, and D. Mironov, 2004: Convective entrainment into a shear-free, linearly stratified atmosphere: Bulk models reevaluated through large eddy simulations. *J. Atmos. Sci.,* **61,** 281–295.

Gentine, P., A. K. Betts, B. R. Lintner, K. L. Findell, C. C. van Heerwaarden, A. Tzella, and F. D'Andrea, 2013: A probabilistic-bulk model of coupled mixed layer and convection. Part I: Clear-sky case. *J. Atmos. Sci.,* **70,** 1543–1556.

Golaz, J., V. Larson, and W. Cotton, 2002a: A PDF-based model for boundary layer clouds. Part I: Method and model description. *J. Atmos. Sci.,* **59,** 3540–3551.

——, ——, and ——, 2002b: A PDF-based model for boundary layer clouds. Part II: Model results. *J. Atmos. Sci.,* **59,** 3552–3571.

Guichard, F., and Coauthors, 2004: Modelling the diurnal cycle of deep precipitating convection over land with cloud-resolving

models and single-column models. *Quart. J. Roy. Meteor. Soc.,* **130,** 3139–3172.

——, L. Kergoat, E. Mougin, F. Timouk, F. Baup, P. Hiernaux, and F. Lavenu, 2009: Surface thermodynamics and radiative budget in the Sahelian Gourma: Seasonal and diurnal cycles. *J. Hydrol.,* **375,** 161–177.

Heus, T., and Coauthors, 2010: Formulation of the Dutch Atmospheric Large-Eddy Simulation (DALES) and overview of its applications. *Geosci. Model Dev.,* **3,** 415–444.

Holland, J., 1971: BOMEX sea–air interaction program and results to date. *Bull. Amer. Meteor. Soc.,* **52,** 926–928.

Jakob, C., and A. Siebesma, 2003: A new subcloud model for mass-flux convection schemes: Influence on triggering, updraft properties, and model climate. *Mon. Wea. Rev.,* **131,** 2765–2778.

Kain, J., and J. Fritsch, 1990: A one-dimensional entraining detraining plume model and its application in convective parameterization. *J. Atmos. Sci.,* **47,** 2784–2802.

Khouider, B., and A. Majda, 2006: A simple multicloud parameterization for convectively coupled tropical waves. Part I: Linear analysis. *J. Atmos. Sci.,* **63,** 1308–1323.

——, J. Biello, and A. J. Majda, 2010: A stochastic multicloud model for tropical convection. *Commun. Math. Sci.,* **8,** 187–216.

Klein, S. A., and D. Hartmann, 1993: The seasonal cycle of low stratiform clouds. *J. Climate,* **6,** 1587–1606.

Lintner, B. R., P. Gentine, K. L. Findell, F. D'Andrea, A. H. Sobel, and G. D. Salvucci, 2013: An idealized prototype for large-scale land–atmosphere coupling. *J. Climate,* **26,** 2379–2389.

Majda, A. J., and S. N. Stechmann, 2008: Stochastic models for convective momentum transport. *Proc. Natl. Acad. Sci. USA,* **105,** 17 614–17 619.

McCaa, J., and C. Bretherton, 2004: A new parameterization for shallow cumulus convection and its application to marine subtropical cloud-topped boundary layers. Part II: Regional simulations of marine boundary layer clouds. *Mon. Wea. Rev.,* **132,** 883–896.

Neggers, R. A. J., 2009: A dual mass flux framework for boundary layer convection. Part II: Clouds. *J. Atmos. Sci.,* **66,** 1489–1506.

——, M. Koehler, and A. C. M. Beljaars, 2009: A dual mass flux framework for boundary layer convection. Part I: Transport. *J. Atmos. Sci.,* **66,** 1465–1487.

Raymond, D., and A. Blyth, 1986: A stochastic mixing model for nonprecipitating cumulus clouds. *J. Atmos. Sci.,* **43,** 2708–2718.

Revercomb, H., and Coauthors, 2003: The ARM program's water vapor intensive observation periods—Overview, initial accomplishments, and future challenges. *Bull. Amer. Meteor. Soc.,* **84,** 217–236.

Siebesma, A. P., and Coauthors, 2003: A large eddy simulation intercomparison study of shallow cumulus convection. *J. Atmos. Sci.,* **60,** 1201–1219.

——, P. M. M. Soares, and J. Teixeira, 2007: A combined eddy-diffusivity mass-flux approach for the convective boundary layer. *J. Atmos. Sci.,* **64,** 1230–1248.

Simpson, J., and V. Wiggert, 1969: Models of precipitating cumulus towers. *Mon. Wea. Rev.,* **97,** 471–489.

——, R. H. Simpson, D. A. Andrews, and M. A. Eaton, 1965: Experimental cumulus dynamics. *Rev. Geophys.,* **3,** 387–431.

Soares, P., P. Miranda, A. Siebesma, and J. Teixeira, 2004: An eddy-diffusivity/mass-flux parametrization for dry and shallow

cumulus convection. *Quart. J. Roy. Meteor. Soc.,* **130,** 3365–3383.

Stevens, B., 2006: Bulk boundary-layer concepts for simplified models of tropical dynamics. *Theor. Comput. Fluid Dyn.,* **20,** 279–304.

Stull, R. B., 1985: A fair-weather cumulus cloud classification scheme for mixed-layer studies. *J. Climate Appl. Meteor.,* **24,** 49–56.

——, 1988: *An Introduction to Boundary Layer Meteorology.* Springer, 666 pp.

Tiedtke, M., 1989: A comprehensive mass flux scheme for cumulus parameterization in large-scale models. *Mon. Wea. Rev.,* **117,** 1779–1800.

von Salzen, K., and N. McFarlane, 2002: Parameterization of the bulk effects of lateral and cloud-top entrainment in transient shallow cumulus clouds. *J. Atmos. Sci.,* **59,** 1405–1430.

Zhu, P., and B. Albrecht, 2002: A theoretical and observational analysis on the formation of fair-weather cumuli. *J. Atmos. Sci.,* **59,** 1983–2005.